Materials and Design 51 (2013) 729–741

Contents lists available at SciVerse ScienceDirect

Materials and Design

journal homepage: www.elsevier.com/locate/matdes

A numerical investigation on explosive fragmentation of metal casing using Smoothed Particle Hydrodynamic method

Kong Xiangshao *, Wu Weiguo, Li Jun, Liu Fang, Chen Pan, Li Ying

Department of Structural Engineering, School of Transportation, Wuhan University of Technology, Wuhan 430063, China

ARTICLE INFO

Article history:
Received 29 January 2013
Accepted 12 April 2013
Available online 28 April 2013

Keywords:
Explosive fragmentation
Metal casing
Fragment distribution
Smoothed Particle Hydrodynamics

ABSTRACT

Explosively driven fragmentation of ductile metals is a highly complex phenomenon. It is an important issue in a variety of circumstances like structure protection, weapon effectiveness and safety distance. Simulations of the fragmentation of metal casing are characterized by a number of interesting and challenging behaviors. These include the volume expansion of the solid charge and its transformation into highly pressurized products. This rapid pressurization of the metal case leads to large deformations at high strain rates and eventual casing rupture. Once the metal casing breaks apart, the highly pressurized product escapes from the gap of the failing casing and generates a shock wave. In addition, the fragments from the metal casing scatter with high velocities in set directions. In the conditions of near field explosion, the spatial distribution of fragments with powerful penetrability has considerable influence on the failure pattern of the target. In the present study, the finite difference engineering package AUTODYN combined with Smoothed Particle Hydrodynamics (SPH) method is used to investigate numerically the fragmentation process of a cylindrical metal casing with ends. After applying the numerical method to predict the propagation of detonation wave, the expansion and rupture process, the expansion velocity of metal casing, the leakage of detonation products and the fragment distribution, the fragment mass distribution is validated by comparing the numerical results with experimental data in the literature. Additionally, an experiment was conducted with the same explosive fragmentation geometry as modeled. The characteristics of the observed fragment distributions and fragment velocities are compared with the numerical simulation. The results reveal that the path of detonation wave is directly related to the expansion velocity of the casing. The fragment sizes depend on the axial position on the casing when the charge is detonated at endpoint, and they are related to the relative axial strain rate. The relatively low axial strain rate, especially in the central and further region of the detonating cylindrical casing, is probably the quantity responsible for the larger fragments. The end far away from the initiation point produces more massive fragments with maximum kinetic energy. It has been demonstrated that the numerical method presented here is capable of simulating the explosive fragmentation of a metal casing with ends.

1. Introduction

Explosively driven fragmentation of ductile metals is a very complex phenomenon in which the fragmenting material is plastically deformed by the intense shock followed by high-rate plastic deformation that ultimately leads to fracture. The damage effects from explosively filled metal casings mainly include the fragments and shock wave. In the conditions of near field explosion, the synergistic effects of the shock wave and fragments would be considerable [1,2]. The modeling of the fragmentation process is of importance for design, redesign and efficiency analysis of projectiles. The fragment mass distribution, the initial fragment velocity, as well as the spatial and the shape distributions of fragments, enable the complete characterization of a fragmentation process [3]. The dynamic issue of fragmentation of metal casing has been of interest to many researchers for decades. In 1943, Gurney [4] showed that the initial velocities of metal casing for spheres, cylinders and infinite planes driven by the enclosed high explosives, could be approximated by a function of the ratio M/C, where M is the casing mass and C is the charge mass. The formula was based on the simplified assumptions of uniform gas density, lack of material strength and late release of detonation products. Mott [5] developed a model to predict the number of fractures around the circumference and the fragment mass of a cylindrical pipe-bomb. In his work, two main types of fracture were observed in the bomb and shell casing, including shear fracture, approximately at 45° to the circumference of the casing, and a combination of fibrous fracture (of the same type as at the bottom of the cup and cone fracture in a tensile test) and shear fracture. Based on energy considerations,

* Corresponding author. Tel./fax: +86 27 86551196.
E-mail address: kongxs@whut.edu.cn (X. Kong).

0261-3069/$ - see front matter © 2013 Published by Elsevier Ltd.
http://dx.doi.org/10.1016/j.matdes.2013.04.041

Grady and Hightower [6] developed a model for fragmenting steel casings of high explosive charge, and an equation relating the circumferential spacing to the strain rate, mass density and fracture energy of material was derived. These early works lay the foundation for the field of fragment study that continues to this day. More recently, various numerical methods based on theoretical models and special experimental techniques were developed to study the fragmentation phenomenon. Anderson et al. [7] used a time-dependent two-dimensional finite-difference code to model the fragmenting cylinders. Besides, a theoretical model of gas leakage was developed to simulate the explosive gas leakage around the fragments after the casing breakup. A comparison of the calculation results utilizing the gas leakage model was made against the experimental tests, which were conducted at BRL on cylinders filled with various high explosives [8]. Based on fragmentation code PAFRAG, Gold et al. [9] proposed a method to predict the performance of explosive fragmentation munitions. Arnold and Rottenkolber [10] investigated the fragmentation behavior of very light and heavy casings. In their work, a data collection method which was based on the image processing was outlined and applied to determine the fragment mass distribution of four different shells. In terms of blast impulse from cased charge, Hutchinson presented a novel idea and calculational formulas were derived based on impulse/momentum analysis [11–13]. The literatures on this topic are progressed in the viewpoints of the mechanical performance, fragment-size distribution, fracture strain, and failure mechanisms [14–24].

Many circumstances arise where a much more sophisticated treatment is necessary to predict the fragmentation features accurately over the entire length of a cylinder including the ends. Such calculation may be required to investigate the differences in initiation sites of the high explosive, properties of casing materials, and irregular shapes of casing. However, there are no corresponding theoretical analysis models. Since the cost of experimental tests is usually very high and time-consuming, many efforts have been made to investigate the behavior of metal casing subjected to inner blast load numerically without the need to undertake a large number of experimental tests. Guilkey et al. [25] described an Eulerian–Lagrangian approach for the simulation of explosion of metal container filled with a high explosive. The approach used a finite-volume multi-material compressible Computational Fluid Dynamic (CFD) formulation, within which the solid materials were represented using a particle method known as the Material Point Method. The Eulerian–Lagrangian coupling was commonly used to describe the interaction effect of inner charge and metal casing in the study of this field [26–28]. But problems exist in the Lagrangian process to simulate the fragmentation of metal casing. When a shell or bomb filled with explosive detonates, the casing is subjected initially to an extremely high pressure from the detonation products. Under this pressure the casing begins to move rapidly outwards. For the case of a ductile material such as steel, very considerable plastic expansion, as much as 50%, occurs before the casing breaks [5]. Besides, the ends of the metal casing have influence on the expansion of the cylinder. The metal casing will deform severely in the fragmentation process. So in the numerical simulation, the Lagrangian grid of metal casing will be severely distorted, and this can lead to the interruption of the numerical process. Although some useful numerical techniques such as erosion algorithms can be used to overcome the problem of grid distortion in the Lagrangian process, it should be noted that the erosion algorithms do not attempt to model the physics of the problem but introduce a numerical palliative to overcome the problems associated with the mesh distortions caused by the gross motions of the Lagrangian grid [29].

Simulations of explosively driven fragmentation of ductile metals are characterized by a number of interesting and challenging behaviors, including the volume expansion of the solid charge and its transformation into highly pressurized products. This rapid pressurization leads to the large deformation and eventual rupture of the metal casing at high strain rates. Once the metal casing breaks apart, the highly pressurized products escape from the gap of the failing casing and generate the shock wave [25]. It is attractive to set up a numerical method, by which the fragment mass distribution, the initial fragment velocity, along with the spatial and the shape distributions of fragments from the metal casing can be reproduced appropriately. In the present study, the finite difference engineering package AUTODYN with Smoothed Particle Hydrodynamics (SPH) method is used to investigate the fragmentation process of cylindrical metal case with flat ends numerically. The outline of the paper is as follows:

(1) In Section 2, the computational procedure is presented. The SPH method is briefly introduced and the numerical model of cylindrical metal case with ends is described.
(2) The numerical results and discussions are presented in Section 3. The propagation of detonation wave, the expansion and rupture process, the leakage of detonation products, the characteristics of the fragment mass distribution and the initial fragment velocity, along with the spatial and the shape distributions of fragment of the metal casing are studied in detail.
(3) For validation purpose, a fragmentation experiment of a metal casing with flat ends was also conducted. The fragment distribution and the characteristic of fragment velocity of the metal casing with ends are compared with the numerical results. The applicability of the numerical method in computing the fragments mass distribution is validated by comparing the numerical results with the experimental data in the literature.
(4) In the last section, some conclusions of the explosive fragmentation process are drawn.

2. Computational procedure

2.1. The SPH method

The SPH method is based on a gridless Lagrangian hydrodynamics using particles. The most attractive feature of SPH method is that it gets rid of the computation termination due to the possible large element distortion inherent in other Lagrangian formulation based on finite element methods. Its applications include astronomical science, hypervelocity impact and super-fast large deformation problems [30–35]. The special feature of the SPH method is very attractive for solving the problem concerning the large deformation.

In SPH method, the fluid is represented by a finite set of observation points or particles, through the use of a smoothing procedure in which the value $\hat{f}(x)$ of function $f(x)$ at a point x, in the domain Ω, is approximated by the integral interpolation [31,36]:

$$\hat{f}(x) = \int_{\Omega} f(x')W(x - x', h)dx' \tag{1}$$

where $W(x - x', h)$ is a smooth function, commonly referred to as the interpolating kernel, and h is the bandwidth of the kernel, or the smoothing length corresponding to the mesh size in FEM analysis. The kernel function is defined such that (i) it mimics the Dirac δ-function in the limit $h \to 0$, $\lim_{h\to 0} W(x - x', h) = \delta(x - x')$, (ii) its integral over the domain Ω is exactly unity, $\int_{\Omega} W(x - x', h)dx' = 1$, and (iii) $W(x - x', h) = W(x' - x, h)$.

Derivatives of $\hat{f}(x)$ are integrated using the kernel function as:

$$\nabla\hat{f}(x) = \int_{\Omega} f(x')\nabla W(x - x', h)dx' \tag{2}$$

By introducing a volume weight m^j/ρ^j for each particle, the discrete forms of mass, momentum, and energy conservation equations of SPH formulation are expressed respectively as follows [36]:

$$\frac{d\rho^i}{dt} = \rho^i \sum_{j=1}^{N} \frac{m^j}{\rho^j}(v_\alpha^j - v_\alpha^i)\frac{\partial W^{ij}}{\partial x_\alpha^i} \tag{3}$$

$$\frac{dv_\alpha^i}{dt} = -\sum_{j=1}^{N} m^j \left(\frac{\sigma_{\alpha\beta}^i}{\rho^{i2}} + \frac{\sigma_{\alpha\beta}^j}{\rho^{j2}}\right)\frac{\partial W^{ij}}{\partial x_\beta^i} \tag{4}$$

$$\frac{dE^i}{dt} = -\frac{\sigma_{\alpha\beta}^i}{\rho^{i2}} \sum_{j=1}^{N} m^j (v_\alpha^i - v_\alpha^j)\frac{\partial W^{ij}}{\partial x_\beta^i} \tag{5}$$

where $W^{ij} = W(x^i - x^j, h)$, t denotes the time, x is the spatial coordinate, ρ is the density, v_α is the velocity component, $\sigma_{\alpha\beta}$ is the stress tensor component, E is the specific internal energy, and the subscripts α ($\alpha = 1, 2, 3$) and β ($\beta = 1, 2, 3$) are the component indices.

Simulation solutions are obtained by solving Eqs. (3)–(5) in conjunction with the material models as well as the initial and boundary conditions.

2.2. Numerical model

The numerical model is developed with the finite difference engineering package AUTODYN. This software is particularly suitable for the nonlinear dynamic problems, such as impact or explosion. It allows for the application of different algorithms such as Euler–Lagrangian, Arbitrary Lagrange Euler (ALE) and SPH to solve the fluid–structure problems. In order to reproduce the explosive fragmentation process, in which the casing material is plastically deformed and eventually ruptured by the inner charge, the SPH method is adopted to model the phenomenon of explosively driven fragmentation.

The object of numerical investigation in this paper is the cylindrical metal casing filled with TNT charge, as shown in Fig. 1. The metal casing described here is fabricated from steel A235, the internal diameter of the cylindrical casing is 110 mm, the length is 160 mm, and the thickness is 6 mm. It is noted that the portions of cylindrical casing with a length of 10 mm adjacent to both ends are thickened to 10 mm. These parts are hereinafter referred to as the thickened part. The ends near to and far away from the initiation point of charge are called near end and far end, respectively. The mass of metal casing is 4.10 kg, with a 1.9 kg TNT charge inside it. The explosive is initiated at one end of the center-line.

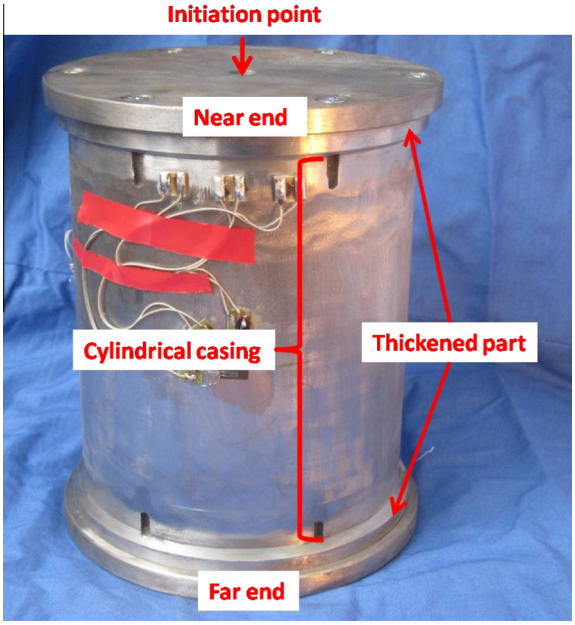

Fig. 1. The cylindrical metal casing with ends.

The symmetry of the problem under consideration allows modeling only a quarter of the whole metal casing and TNT charge, as shown in Fig. 2. Since the nature of this simulation demands a very high mesh density, such a reduction in the model size is very desirable. Both the metal casing and the TNT charge inside the casing are discretized by means of a set of particles which are assigned with a mass interacting among themselves without direct connectivity. The SPH method requires a large number of particles uniformly distributed to provide reasonably accurate results. The size of particles depends on two factors, the smallest fragment mass and the time step of the numerical process, which influences each other. In AUTODYN, the minimal fragment is composed at least two particles. Thus the size of the particles should be as small as possible to reflect the fragment mass distribution of the metal casing appropriately. On the other hand, if the size of particles is too small, the numerical process is time-consuming or even be interrupted. In present study, several different particle sizes were studied and finally a diameter of 1.0 mm was chosen, resulting in 513,192 particles, and the smallest fragment mass is 0.066 g, which is enough to count the fragment mass distribution. The simulations are carried out in a workstation with eight dual core processors, and the parallel processing environment is established to improve the efficiency.

2.3. Equation of state of metal casing

The Shock Equation of State (EOS) adopts the Mie-Gruneisen EOS based on the shock Hugoniot of an impact event, which is widely used and adequately represents most materials. This EOS uses the basic relationship between the particle velocity and the shock velocity $U = c_0 + su_p$, with the form shown as follows:

$$p = p_H + \Gamma\rho(e - e_H) \tag{6}$$

where it is assumed that $\Gamma\rho = \Gamma_0\rho_0 =$ constant, Γ_0 is the Gruneisen coefficient, ρ and ρ_0 are current density and initial density, respectively. The variables p_H and e_H are given by:

$$p_H = \frac{\rho_0 c_0 u(1+u)}{[1-(s-1)u]^2} \tag{7}$$

$$e_H = \frac{p_H}{2\rho_0}\left(\frac{u}{1+u}\right) \tag{8}$$

where $u = (\rho/\rho_0) - 1$, c_0 is the bulk sound speed, s is a material parameter to be determined experimentally. For steel the values taken for c_0 and s were 4569 m/s and 1.49, respectively from [33].

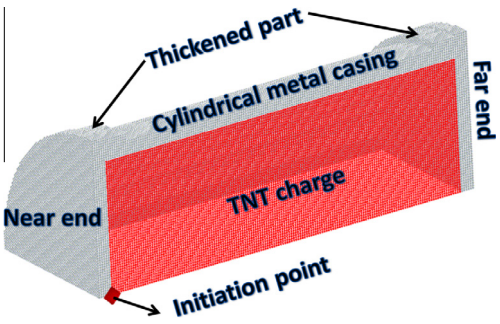

Fig. 2. 1/4 Computational model of the metal casing and TNT charge.

A limitation of this EOS is that it is only applicable for a limited impact velocity range, as it does not allow for any material phase changes such as melting or vaporization [37].

2.4. Strength model and failure criterion of metal casing

The rapid pressurization leads to the large deformations and eventual rupture of the metal casing at high strain rates. The Johnson–Cook constitutive relation [38] is selected to model the material behavior of the metal casing.

$$\sigma = (A + B\varepsilon_p^n)(1 + C\ln\dot{\varepsilon}^*)(1 - T^{*m}) \tag{9}$$

where A, B, C, n and m are Johnson–Cook material constants, ε_p is the effective plastic strain, $\dot{\varepsilon}^* = \dot{\varepsilon}_p/\dot{\varepsilon}_0$ the effective plastic strain rate at a reference strain rate $\dot{\varepsilon}_0 = 1\ s^{-1}$ and the homologous temperature $T^* = (T - T_r)/(T_m - T_r)$ where T is the material temperature, T_r is the room temperature, and T_m is the melting temperature of material.

The material parameters used for the Johnson–Cook constitutive relation are listed in Table 1.

The fragmentation of the casing occurs due to the local failure in the casing material. Real materials have inherent microscopic flaws and it is at these flaws that the failure and cracking initiate. The exact distribution and type of these flaws depend on the type of material considered, the material formation process and any post-forming treatments applied to the material. However, these details cannot be resolved in a numerical mesh, so a statistical approach is required to account for an inherent flaw distribution. The method taken is to characterize the failure strain of the casing material according to a random distribution. Each cell in the numerical model has a slightly different strain at which the cell will fail. This makes the material contain weak spots, at which the failure will be expected to initiate [26]. The failure mode should be defined in the AUTODYN to provide a suitable failure criterion for the casing material. In the present study, the principal strain failure model and stochastic failure material model based on the Mott distribution is used to simulate the formation of natural fragments.

Mott [5] assumes that the chance that an unfractured specimen with unit length will fracture when the strain increases from ε to $\varepsilon + d\varepsilon$ is:

$$Ce^{\gamma\varepsilon}d\varepsilon \tag{10}$$

where C and γ are constants. The exponential expression is chosen as the simplest form which gives a rapid increase from negligible to a large value as ε increases. With this assumption, the chance p that the specimen breaks before the strain ε is reached can be obtained by:

$$dp = (1 - p)Ce^{\gamma\varepsilon}d\varepsilon \tag{11}$$

where $(1 - p)$ is the probability that there is no fracture for the strain value less than ε.

Considering the initial condition $\varepsilon = 0$, $p = 0$, the solution of Eq. (11) yields the failure probability p at the strain ε:

$$p = 1 - \exp\left\{-\frac{C}{\gamma}(e^{\gamma\varepsilon} - 1)\right\} \tag{12}$$

The average fracture strain ε_0 is given by:

$$\varepsilon_0 = \int_0^\infty \varepsilon\frac{dp}{d\varepsilon}d\varepsilon = \frac{1}{\gamma}\left\{\log\left(\frac{\gamma}{C}\right) + \bar{\varepsilon}\right\} \tag{13}$$

where $\bar{\varepsilon} = \int_{-\infty}^{\infty} xe^x\exp(-e^{-x})dx = 0.577$.

The standard deviation of the critical strain value is:

$$\sigma_\varepsilon = \left(\int_0^\infty (\varepsilon - \varepsilon_0)^2 dp\right)^{1/2} = \frac{1}{\gamma}\frac{\pi}{\sqrt{6}} \approx \frac{1.282}{\gamma} \tag{14}$$

Mott shows that the parameter γ, which is directly related to the fracture strain deviation, can be approximated by the function of the mechanical characteristics of material, as:

$$\gamma \approx 160\frac{P_2}{P_F(1 + \varepsilon_F)} \tag{15}$$

where P_F is the true ultimate stress, ε_F is the plastic strain at fracture, and the parameter P_2 is the proportionality coefficient in the strain-hardening law for the material at high strains, $P = P_1 + P_2\log(1 + \varepsilon)$.

In this paper, the material properties of the mild steel used to manufacture the casing are obtained from the standard tensile tests, as shown in Fig. 3. The corresponding parameters $P_2 = 375$ and $P_F = 530$ MPa are obtained from the test data.

The plastic strain at fracture of the specimens is defined by the reduction in area:

$$\varepsilon_F = -2\ln\left(\frac{d_{\text{final}}}{d_{\text{initial}}}\right) \tag{16}$$

where d_{final} is the final diameter after the specimen breaks, and d_{initial} is the initial diameter.

According to Eq. (16) and test data, the average plastic strain at fracture of the specimens is 0.988. Thus, the value of γ can be determined by Eq. (15), and $\gamma = 57$. The average principal tensile failure strain determined in the tensile test is 0.3. In the AUTODYN code, the value of principal tensile failure strain of the principal strain failure model and the parameter of the stochastic failure material model chosen for the failure criterion of metal casing in the present numerical study are 0.3 and 57, respectively.

2.5. EOS of TNT

A standard JWL (Jones–Wilkins–Lee) equation of state is employed to describe the adiabatic expansion of the detonation products. The equation represents the pressure as a function of the volume and energy:

$$p_T = C_1\left(1 - \frac{\omega}{r_1 v}\right)e^{-r_1 v} + C_2\left(1 - \frac{\omega}{r_2 v}\right)e^{-r_2 v} + \frac{\omega e}{v} \tag{17}$$

where C_1, C_2, r_1, r_2 and ω are constants. p_T, v and e are the pressure, relative volume and specific internal energy, respectively.

The material properties and parameters used for the JWL equation are shown in Table 2.

3. Calculational results and discussions

3.1. Propagation of detonation wave

When the explosive is initiated at one end of the center-line, the detonation wave travels outward from the initiation point and then is reflected by the wall of the casing, as shown in Fig. 4. Fig. 4a–c shows that the wave reaches the cylindrical wall of the casing and then reflects with the further development of the detonation process. As a result of the pressure of the side-on detonation wave, the near end (referring to Fig. 1) begins to deform along its normal direction. The cylindrical casing deforms outward under the high pressure of the detonation wave. As a result of the inci-

Table 1
Johnson–Cook parameters of A235 steel.

Material	A (MPa)	B (MPa)	n	C	m
A235 steel	249.2	45.6	0.875	0.32	0.76

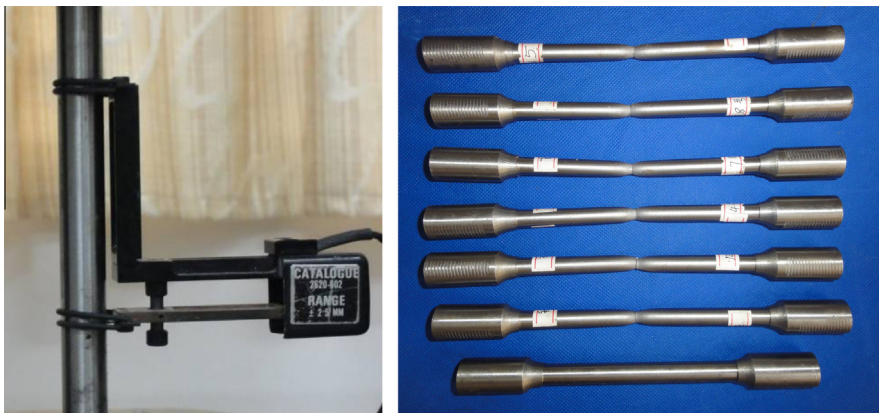

Fig. 3. Standard tensile tests of material specimens.

Table 2
JWL EOS parameters of TNT.

Density ρ (kg/m^3)	Detonation velocity D (m/s)	C–J pressure (Pa)	C_1 (Pa)
1630	6800	2.10E+10	3.74E+11
C_2(Pa)	r_1	r_2	ω
3.75E + 9	4.15	0.9	0.35

dent detonation wave interacting with the reflected wave near the cylinder wall, a high pressure region is formed and travels along the wall of the cylindrical casing subsequently. It is noticeable that another high pressure region which is colored red appears and moves along the center-line to the far end, as shown in Fig. 4d–j. The high pressure region results from the convergence effect of the reflected wave from the cylindrical casing, because the casing is rotationally symmetric to the geometry center. Immediately after the initial free wave reaches the far end, the reflected wave from the cylindrical casing impinges on the far end. Besides, the far end will be attacked by the converged wave of the reflected waves from cylindrical casing once again. These waves will be reflected once more from the far end, thus the additional driving force will bring to bear on the portion of the cylindrical casing close to the far end. As the time goes on, the volume of detonation products increases continuously, and the intensity of the subsequent reflected wave decreases dramatically. As a result, the reflected waves from the far end have less influence on the near end and the part of the cylindrical casing near to the initiation point.

3.2. Expansion and rupture process

In the numerical simulation, the volume expansion of the TNT charge and its transformation into highly pressurized products drives the metal casing to expand and eventually rupture. At the beginning, the material of the metal casing is elastic. When the material's yield strength is exceeded, the casing deforms plastically and finally fails based on the maximum principal tensile failure strain in the cell. The expansion and rupture process of the metal casing at different times are shown in Fig. 5, in which Fig. 5a–r are the scale of the images reduced to fit the frames as the simulation expands, Fig. 5s–v are actual scales of images at certain time. At the very start, the end of the casing adjacent to the initiation point begins to deform outward in its normal direction, and the adjacent cylindrical casing expands radially. However, the expansion radii of the cylindrical casing are different along the axis of the cylinder. Subsequently, the near end breaks from the casing and flies away. It can be seen from Fig. 5c that at the time of $t = 5.30 \times 10^{-2}$ ms the fracture appears on the cylindrical casing and runs parallel to the axis of the cylinder, until to the end. With the increase of the cylinder radius, more parallel fractures appear. The distances between the circumferential cracks determine the width of the fragments. Compared to the near end, the far end is torn rapidly from the metal casing and flies away more quickly, as can be seen from Fig. 5c–r. Both ends deform as bowl-shaped, and the fragments are produced under the circumstance of great curvature of 'bowl-ends'. It is apparently observed that the expansion radii of the joint parts between both ends and the cylindrical casing are smaller. There are massive small particles appearing at the joints between two ends and the cylinder, especially at the joint close to the far end. The most striking feature of the expansion and rupture process is the fragment formation in the axial direction. The axial spacing determines the length of fragments. After the near end departs from the casing, the thickened part of the cylinder is torn and a cylindrical ring is formed. Accompanied by the circumferential expansion, the cylindrical ring fractures and yields the fragments. The condition is quite the same as the thickened part adjacent to the far end. The major difference is that many axial cracks appear and the independent fragments are produced along the cylinder from the un-thickened portion close to the initiation point. With the increase of the expansion, the radius of the cylinder increases along the axial direction, as shown clearly in Fig. 5r, and more axial fractures appear. It is quite interesting that the expansion radius of the cylindrical casing near the initiation point is smaller than that far away from the initiation point. But more fragments with smaller length are produced at the location adjacent to the initiation point, while more massive fragments with higher velocity are from the far away location.

3.3. The leakage of detonation products

The leakage of detonation products is an interesting phenomenon in the fragmentation process of metal casing, and the highly pressurized detonation products escape from the gap of the failing casing. In this section, the leakage phenomenon is presented in detail.

In a short while after the charge is detonated, the near end is broken away from the casing, and the detonation products escape from the gap, as shown in Fig. 6a. At this moment, the circumferential cracks appear on the cylinder. However, no explosive particles escape, and the casing does not reach a high expansion radius in this situation. As cracks increase, the leakage of detonation products emerges from the cracks on the cylinder, as shown in Fig. 6b and e, which represent the side view and top view at the same time, respectively. When the far end is torn, the detonation prod-

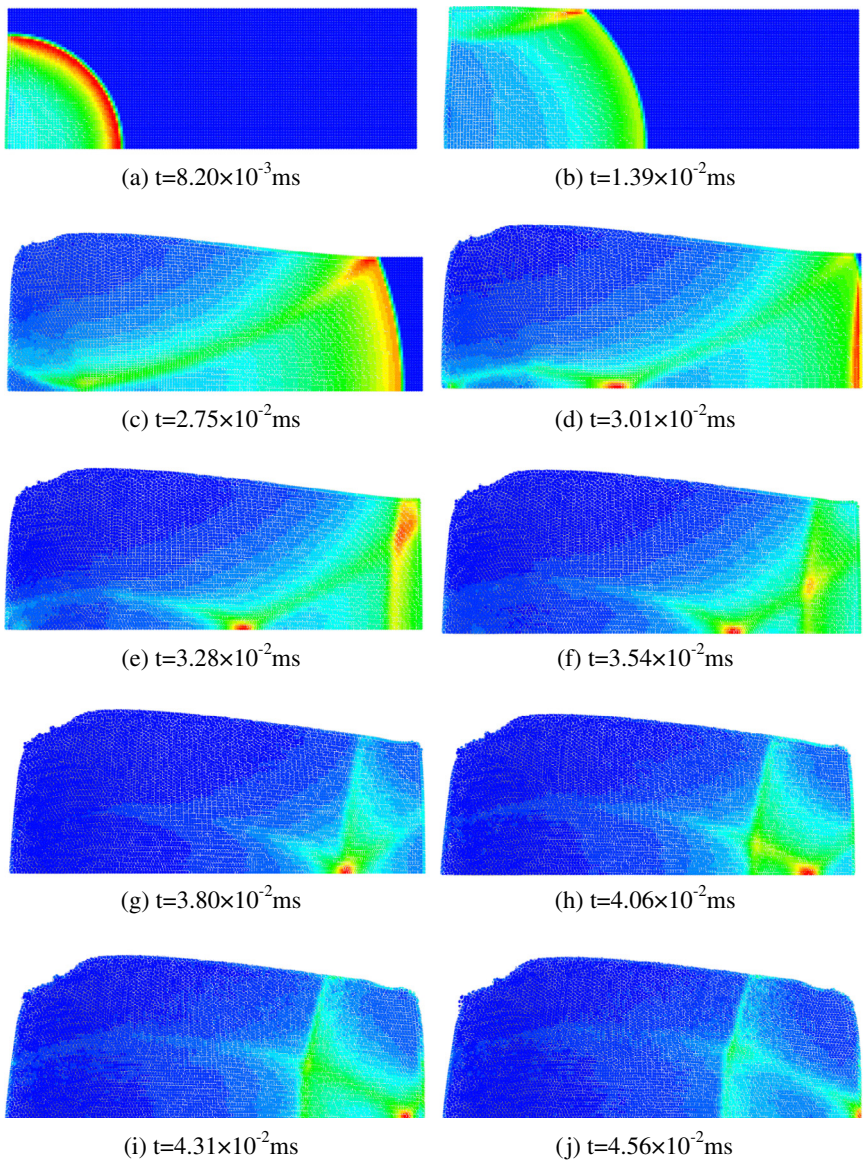

Fig. 4. Propagation of detonation wave.

ucts also escape from the gaps. More and more explosive particles pass through the cracks of the cylinder and the gaps between the ends and the cylindrical casing. Compared to the expansion speed of the cylindrical casing, velocities of these explosive particles are higher. From Fig. 6c, f, d, g, it is found that the gaps between the ends and the cylindrical casing are the main passages of the detonation products. The continuing leakage of the detonation products and the volume expansion lead to the dramatic dropping of the inner pressure, thus the acceleration of the casing reduces accordingly and the expansion velocity tends to become stable. As shown in Figs. 8–10, the expansion velocity of the casing becomes stable at 0.075 ms, at which the explosive particles escape incessantly. It means that under the condition of expansion with stable velocity the inner pressure does not apply on the casing anymore. It should be noted that the influence of air is not considered in the numerical simulation.

3.4. Characteristic of expansion velocity

In the numerical simulation, for the sake of clarity, only some representative points (gauges) are selected on the metal casing surface to obtain the characteristic of expansion velocity, as shown in Fig. 7. Gauges 1–4 are on the near end, gauges 5–8 (5, 6 and 7, 8 are symmetrical in the axial direction) are on the cylindrical casing and gauges 9–12 are on the far end, respectively. It is noted that the gauges 1 and 9 are 5 mm off-axis from the centre point of the ends. Because the velocity on the axis of the cylinder is not representative, and zero mass corresponds to these points.

The velocity–time curves of the gauges on the metal casing are shown in Figs. 8–10. The radial direction is denoted as Y and axial direction is Z. Fig. 8 shows the velocity history of gauges on the near end. In Fig. 8, the symbols $Y_{\mathrm{vel}-1}$ and $Z_{\mathrm{vel}-1}$ stand for the Y-velocity and Z-velocity of gauge 1, respectively. The meanings of the remaining symbols in the other figures may be deduced by analogy.

As soon as the charge is detonated, the near end is accelerated rapidly. The Z-velocity of gauge 1 reaches its maximal value 1323 m/s at 0.05 ms. The Y-velocity of gauge 4 which is located on the edge of the near end is 598.8 m/s and Z-velocity is only 362.3 m/s. The Y-velocities and Z-velocities of gauges 1–3 are much lower and larger than those of gauge 4, respectively. The trend is the same as those of the gauges arranged on the far end,

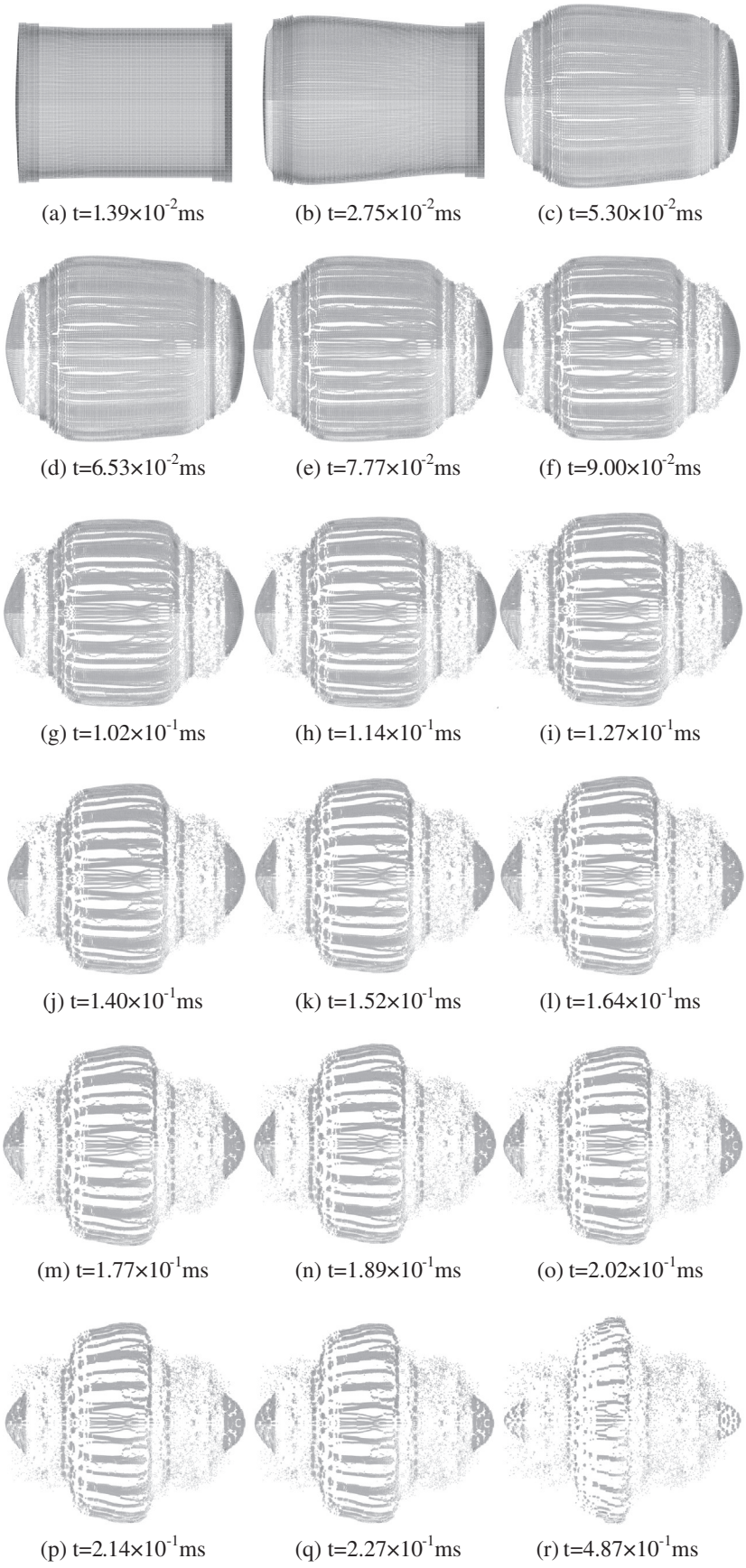

Fig. 5. The expansion and rupture process of the metal casing.

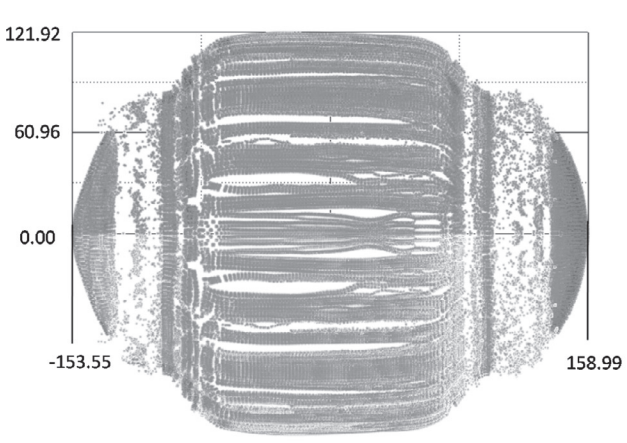

(s) Actual scale t=9.00×10^{-2}ms

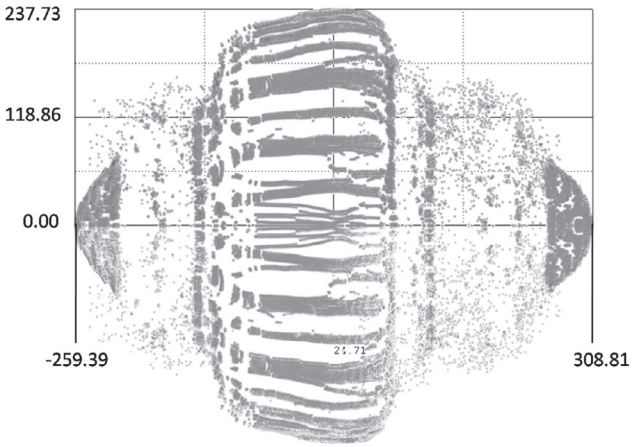

(u) Actual scale t=2.02×10^{-1}ms

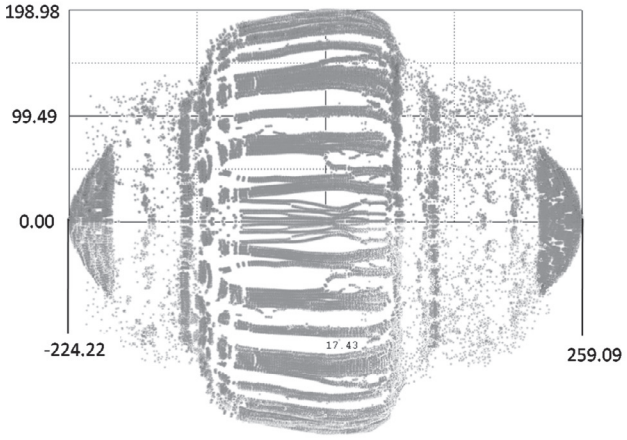

(t) Actual scale t=1.64×10^{-1}ms

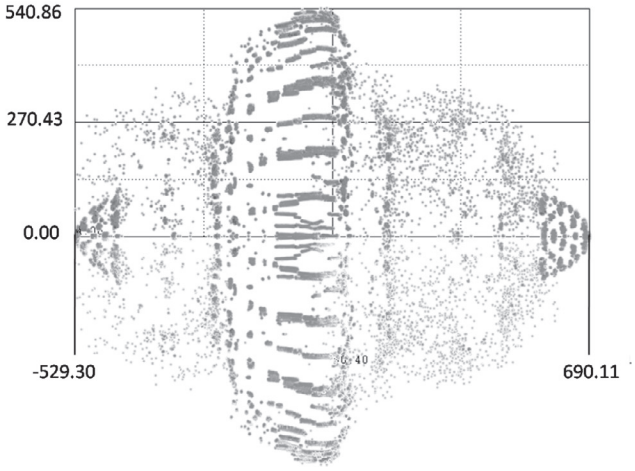

(v) Actual scale t=4.87×10^{-1}ms

Fig. 5. (*continued*)

as shown in Fig. 9. However, the velocities of gauges on the far end increase more rapidly comparing to the gauges on the near end. The maximal Z-velocity of gauge 9 is 1745.1 m/s, while the Y-velocity of gauge 12 is 734.3 m/s. The ratio of Z_{vel-9}/Z_{vel-1} = 1.319, and Y_{vel-12}/Y_{vel-4} = 1.226. The expansion velocity of the far end is higher. As discussed in Section 3.1, the far end is subjected to the repeated reflection waves. Therefore, the additional driving forces apply on the far end and moves rapidly. For the cylindrical casing, under the pressure effect of detonation wave, the gauges' locations begin to move in turn along the axis of the cylinder. The Y-velocity of gauge 5 which is close to the initiation point is lower than those of other gauges. The final velocities of all gauges in the axial direction are in the range from −150 m/s to 150 m/s. The changes of axial velocities of the gauges are mainly due to the influences of the end and the detonation wave propagation.

From the above discussion in Section 3.2, it is found that for the cylindrical casing more fragments with smaller length are produced at the location near to the initiation point, while more massive fragments with higher velocity are from the far away location. Grady and Hightower [6] proposed a method to derive the circumferential fracture spacing, and the circumferential strain rate is $\dot{\varepsilon} = d\varepsilon/dt = V/R_0$ (V and R_0 are the expansion velocity and initial radius of the sample, respectively). According to the expansion velocities of different locations on the cylinder, there is a significant difference between gauges 5 and 6, but the velocities of gauges 7 and 8 are close to each other. It is inferred that the length of the fragment is related to the relative expansion strain rate along the axis of cylinder. The relatively low axial strain rate, especially in the half part of the cylindrical casing far away from the initiation point, is probably the reason responsible for the massive fragments.

3.5. Fragment distribution

The spatial distribution and mass distribution of fragments of the metal casing are shown in Fig. 11a and b, respectively. In the numerical simulation, 2356 fragments are produced, mainly from the cylindrical casing and both ends. The maximum mass of fragments is 36.1 g, produced by the cylindrical casing, with average speed of 1389.1 m/s. It is found that all fragments with mass more than 20 g are produced by the two ends and the part of cylinder approximately 110 mm away from the initiation point (the total length of the cylinder is 160 mm) in the axial direction. The fragments produced from the far end are more attention-getting, for they have higher kinetic energy and stronger penetrability to the target. It has been presented in Section 3.4 that the ratio of velocities in the Z direction between the far end and the near end is Z_{vel-9}/Z_{vel-1} = 1.319.

The predicted mass distribution characteristic of the metal casing is shown in Fig. 11b. In this, the cumulative mass of fragments in the range from 1 g to 10 g is 1832.4 g, and the corresponding values in the range from 10 g to 20 g and from 20 g to 36.1 g are 938.6 g and 606.8 g, respectively. The major part of mass of the

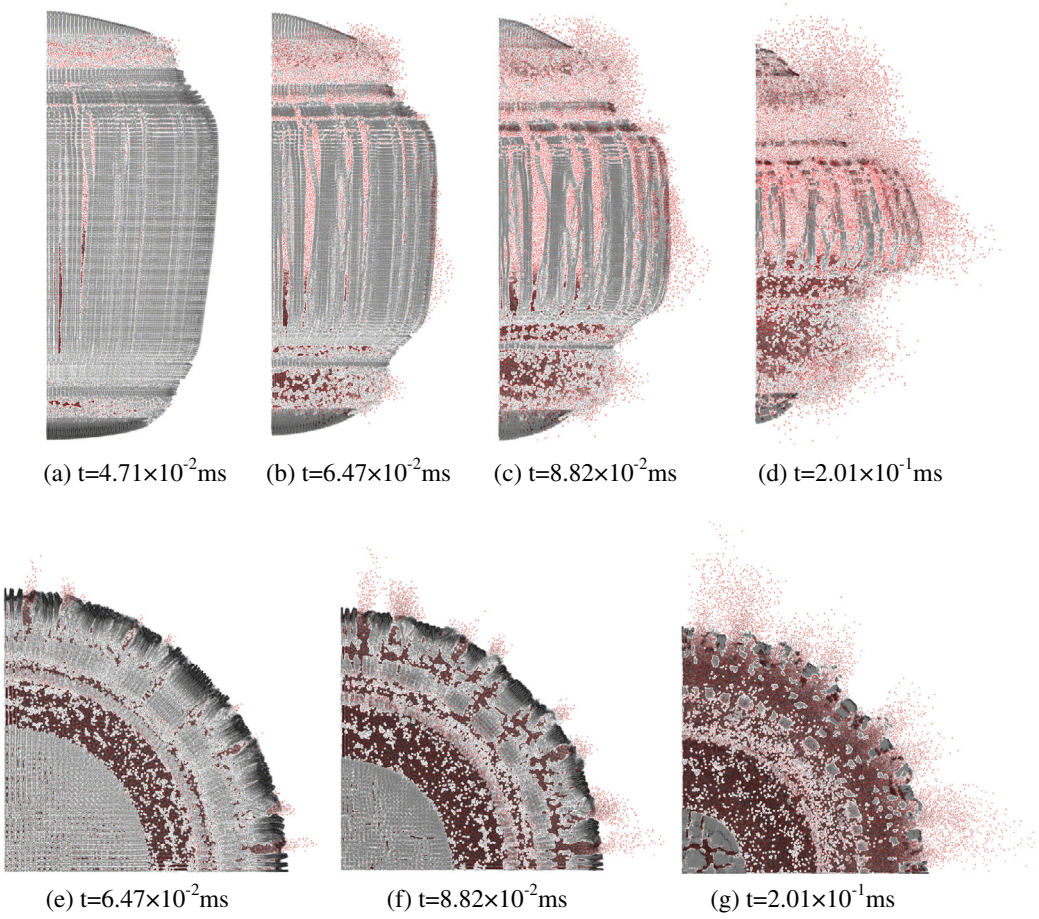

Fig. 6. The leakage of detonation products.

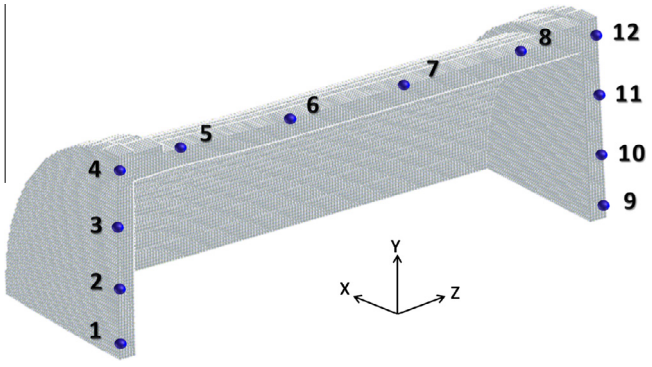

Fig. 7. Representative points selected on the metal casing surface in numerical simulation.

metal casing forms the fragments with mass less than 10 g, and the percentage of the fragments with mass more than 10 g is 40.9%.

4. Experimental comparison

4.1. Comparative analysis

The fragment mass distribution, the initial fragment velocity, along with the spatial and the shape distributions of fragments are the main features of explosive fragmentation of metal casing. In this section, some comparative analysis between the numerical results and the experimental data are made to validate the applicability of the numerical method in modeling the fragmentation of metal casing.

4.2. Spatial distribution and characteristic fragment velocity

In order to investigate the spatial distribution and the velocity characteristic of fragments and compare with the numerical results, an experiment was conducted. In the experiment, the warhead model was arranged in a cabin-like structure and initiated at one end of the center-line, as shown in Fig. 12. This was so the fragment distribution could be clearly represented by checking the perforations on the plates of the cabin-like structure. A high-speed camera was employed to record the experiment process, and the fragment velocities of different locations of metal casing have been approximately determined from the camera images, as will be described later.

The damage and perforations produced by fragments on the structure are shown in Fig. 13. The perforations caused by the fragments from the cylindrical metal casing are shown in Fig. 13a. Since the structure is close to the warhead model, the perforations are concentrated in a narrow band, marked by a red ellipse in Fig. 13a. On the left of the band, there are several perforations with scattered plots, while the perforations do not appear on the right. In the work of Arnold and Rottenkolber [10], this kind of distribution of the fragments from the cylindrical casing can be better illustrated, which is in accordance with the numerical results of the present study. The perforation distributions caused by the near end and far end are shown in Fig. 13b and c, respectively. By

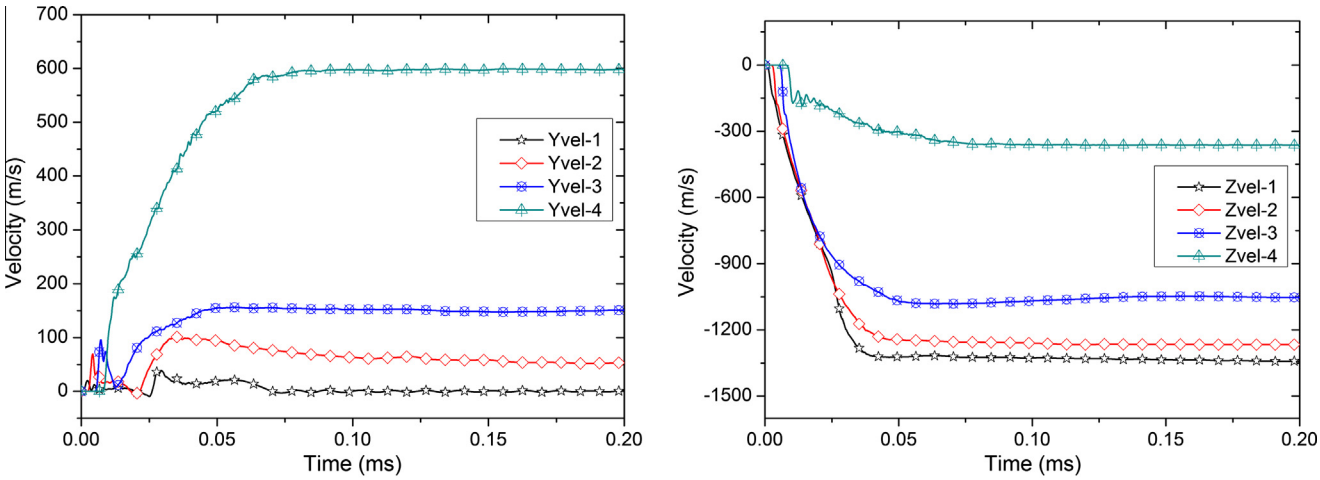

(a) Y-velocity of measuring points (b) Z-velocity of measuring points

Fig. 8. Velocity of measuring points on near-end.

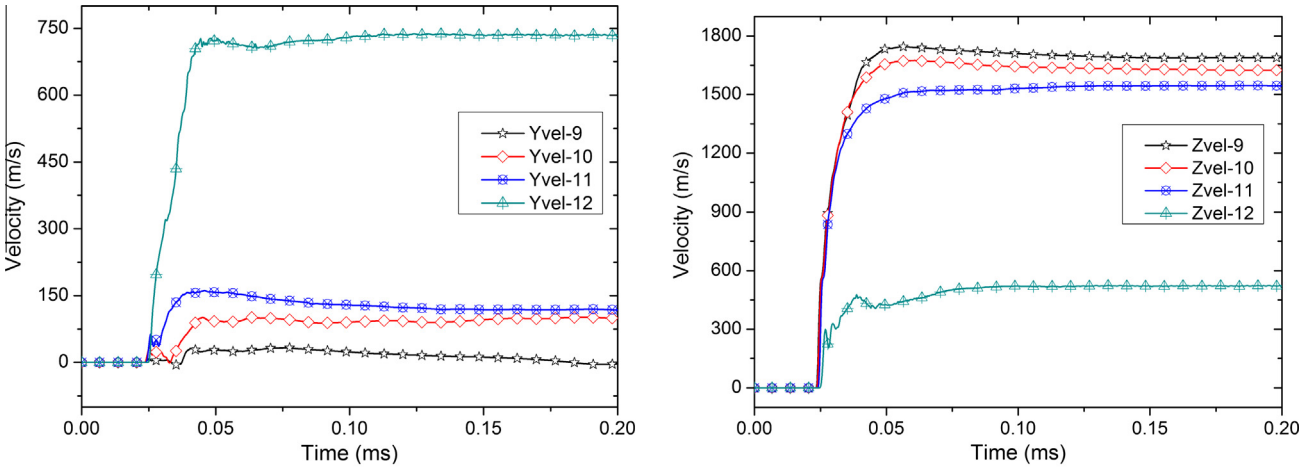

(a) Y-velocity of measuring points (b) Z-velocity of measuring points

Fig. 9. Velocity of measuring points on far-end.

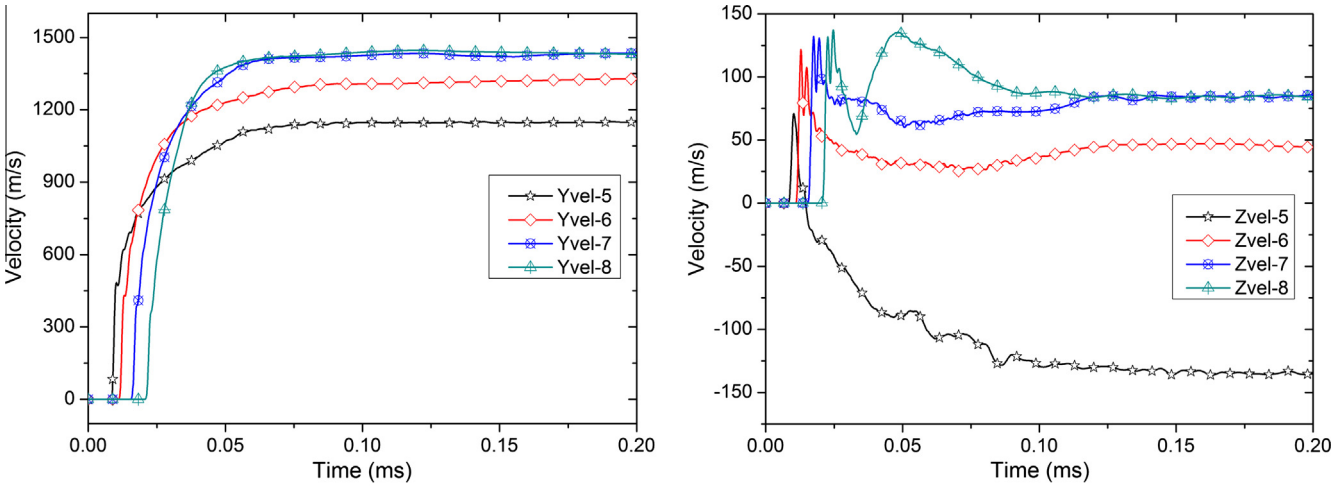

(a) Y-velocity of measuring points (b) Z-velocity of measuring points

Fig. 10. Velocity of measuring points on cylindrical casing.

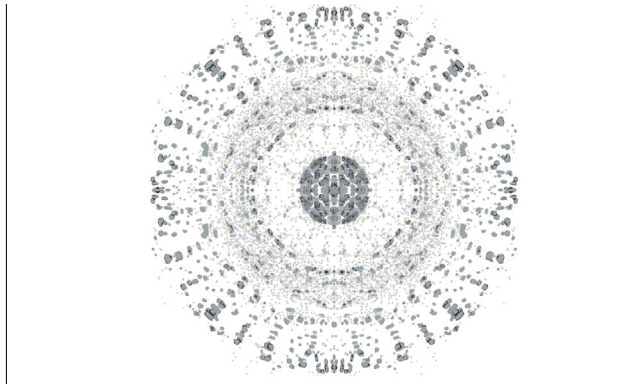

(a) Spatial distribution of fragments

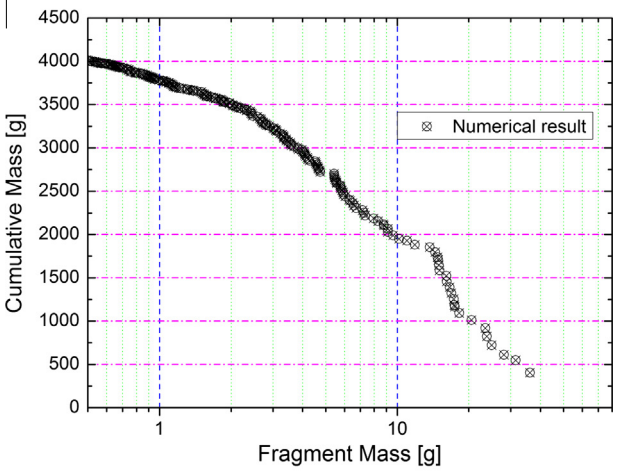

(b) Mass distribution of fragments

Fig. 11. Fragment distribution.

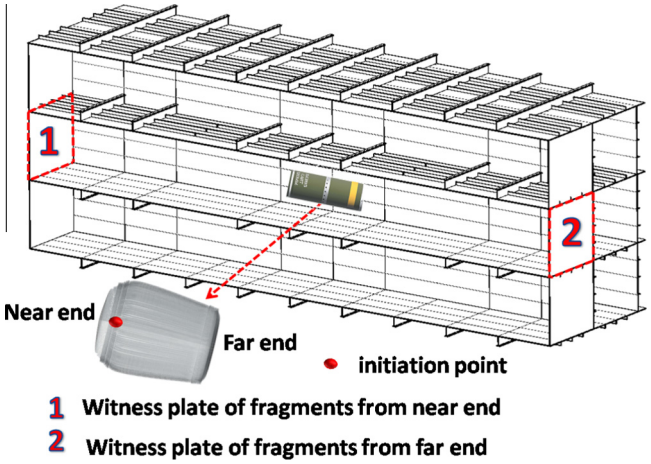

Fig. 12. Arrangement of warhead model.

comparing Fig. 13b and c, it is found that there are more humps appearing on the target plate near to the far end, which are caused by the small fragments that do not penetrate the plate. In the numerical simulation, a number of particles emerge at joint locations between cylindrical casing and two ends. By checking the perforations on the other plates of the structure, it is found that there are few perforations. Besides, the perforations caused by the fragments from two ends are almost concentrated on the square plate with the side length of 600 mm (the lengths of the perforated plates in Fig. 13b and c), and the travel distance of these fragments in the air nearly reaches 2.5 m.

The velocities of fragments are derived from the record of high-speed camera using the time interval and distance between the TNT filled metal casing and the target plate. The target plates near to the ends and cylindrical casing are 2.5 m and 0.9 m away from the center of the metal casing, respectively. The velocities of the three parts of the metal casing measured from the experiment are V_c = 1207 m/s (velocity of fragment from the cylindrical casing), V_n = 1210 m/s (velocity of fragment from the near end), V_f = 1613 m/s (velocity of fragment from the far end). They are smaller than the corresponding numerical results. However, the ratio of velocities of the far end and near end is V_f/V_n = 1.333, which is close to the numerical result Z_{vel-9}/Z_{vel-1} = 1.319. This ratio should be comparable, for in the experiment the travel distances of fragments from near and far end are equal.

The initial velocity of fragment predicted by Gurney is,

$$V_0 = \sqrt{2E}\sqrt{\frac{C/M}{1+0.5C/M}} \tag{18}$$

where $\sqrt{2E} = 520 + 0.28De$, De = 6860 m/s is the detonation velocity of TNT. C and M are mass of TNT and metal casing, respectively.

The initial velocity predicted by Eq. (18) is 1383.8 m/s. In the numerical simulation, the range of expansion velocities along the cylindrical metal casing is from 1187.3 m/s to 1440.2 m/s. But the fragments with maximum velocity are from the far end, with expansion velocity of 1745.1 m/s. It is also observed in the experiment, but cannot be predicted by Gurney formula.

4.3. Mass distribution of fragments

In the experiment mentioned above, the mass distribution of fragments is not obtained due to the lack of suitable capture medium, such as expanded vermiculite mica. Arnold and Rottenkolber [10] used a data collection method to study the fragment mass distribution of four different shells experimentally. In their work, the cylindrical explosive charges with a diameter of 100 mm and a height of 200 mm were used for the test samples. Two half shells with no ends were attached to the charge. The charge was point-initiated from the top. The comparative analysis of fragment mass distribution between the results from numerical method in the present study and the experimental data obtained by Arnold and Rottenkolber is presented.

The comparison of cumulative mass distributions between the experiment data and the numerical result is shown in Fig. 14. The prescribed minimum fragment mass is taken as 1 g for the comparative analysis, in consideration of the difficulty in the collection of smaller fragments in the experiment. The comparison indicates that the numerical results of cumulative mass distribution of the fragments less than 20 g agree well with the experiment data. However, for the more massive fragments, the numerical results are higher than the experiment data. It means that there appear to have been fewer larger fragments produced in the experiment than in the distribution derived from the numerical simulation. Predrag and Slobodan [21] found that the fragment mass distribution of naturally fragmenting warheads could be described by the generalized Mott, the generalized Grady and the Weibull distribution law. Thus, the number and mass of large fragments are relatively limited, which is consistent with the experimental phenomena. The numerical method is capable of predicting the fragment mass distribution of the metal casing to a certain extent.

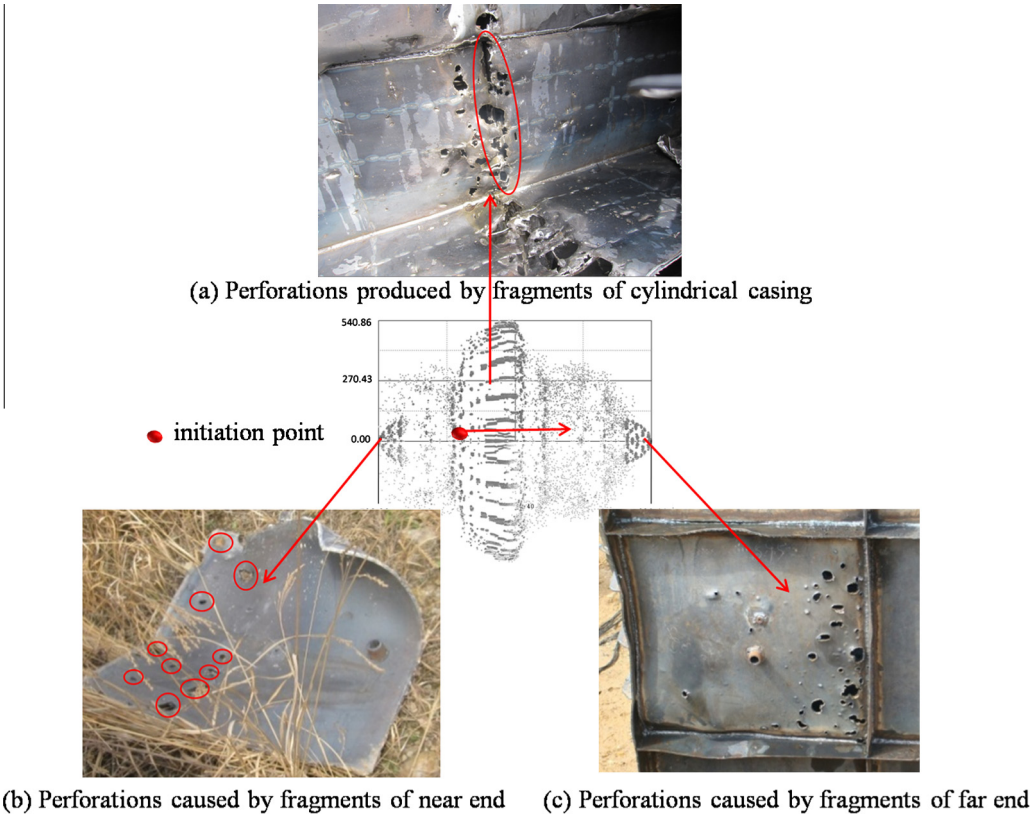

Fig. 13. Perforations produced by fragments.

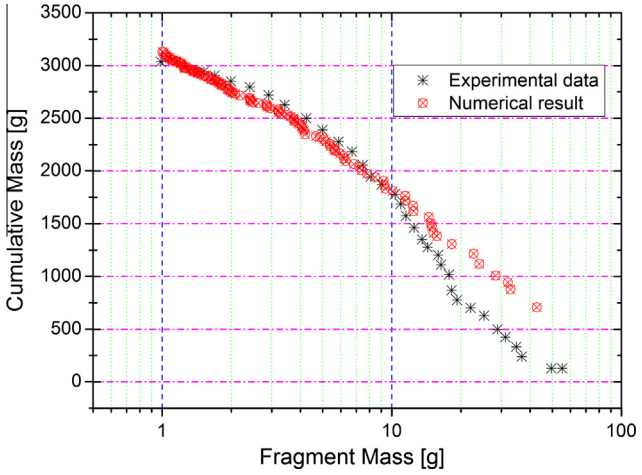

Fig. 14. Comparison of cumulative mass distributions.

5. Conclusions

This study makes it possible to simulate the main features of the explosive fragmentation process of the cylindrical metal casing with ends. The numerical analysis code AUTODYN with SPH method is used to model the propagation of detonation wave, the expansion and rupture process, the expansion velocity of the metal casing, the leakage of detonation products and the fragment distribution.

Simulation results show that the propagation and reflection of the detonation wave has direct relationship to the casing expansion and rupture. The far end has higher velocity in its normal direction than the near end, and the part of the cylinder far away from the initiation point expands more rapidly, which are mainly due to the additive effect of the initial free and reflected detonation waves.

The size of fragments is related to the circumferential and axial spacings of the fractures. The axial fracture spacings of the part of the cylindrical casing closer to the initiation point are smaller, and more fragments are produced when the expansion radius is relatively small. The part of the cylindrical casing far away from the initiation point yields less axial fracture in the condition of larger expansion radius, but more massive fragments are produced. Meanwhile, there is little difference among the circumferential fracture spacings along the whole axial direction of the cylinder. Considering the expansion velocity characteristic of cylindrical casing, it is evident that the fragment size is related to the relative axial strain rate. The relatively low axial strain rate, especially in the half part of the cylindrical casing far away from the initiation point, is probably the reason responsible for more massive fragments.

The detonation products escape from the fracture spaces of the metal casing, thus the inner pressure is reduced. From the results of numerical simulation, it is found that the detonation product begins to escape from the fracture gaps between the near end and the cylinder before the leakage from the fracture spacings of the cylinder appears. The gaps between the ends and the cylinder are the main thoroughfares of the detonation products.

When the warhead detonates, a large number of small particles are produced at the joint parts between the cylindrical casing and the two ends, and more massive fragments are produced from the region of the cylinder approximately 110 mm away from the initiation point and the two ends of the metal casing. The fragments with maximum kinetic energy are from the far end, with velocity of 1.3 times higher than that of the fragments produced by the near

end. Numerical results of the fragment velocity and distribution characteristic are in agreement with the experimental data. Special attention should be paid to those fragments with more powerful penetrating capability in the design of protective structures.

The numerical method present in this paper should be further validated by artfully designed experiments to investigate the influence of properties of casing materials on fragmentation. In future, the authors intent to conduct X-ray experiments to obtain the detailed information about the expansion and rupture process of cylindrical metal casing with ends. Additionally, development of a soft-recovery method remains a task for future activities.

Acknowledgments

The authors thank Prof. Arnold and Prof. Rottenkolber for providing the experimental data of fragment mass distribution of metal cased explosive charge. Prof. Zhu Xi and Dr. Hou Hai-liang are thanked for their valuable help during experimental testing. This work was done with the financial support of the Defense Industrial Technology Development Program reference A1420080184, and of the Fundamental Research Funds for the Central Universities reference 2011YB08.

References

[1] Joosef L. Experiments and numerical analyses of blast and fragment impacts on concrete. Int J Impact Eng 2005;31(7):843–60.
[2] Marchand KA, Vargas MM, Nixon JD. The synergistic effects of combined blast and fragment loadings, in Southwest Research Institute Final Report No. ESL-TR-91-18 to Air Force Engineering & Services Center, Florida; 1992.
[3] Elek P, Jaramaz S. Fragment mass distribution of naturally fragmenting warheads. FME Trans 2009;37:129–35.
[4] Gurney GW. The initial velocities of fragments from bombs, shells and grenades. Ballistics Research Laboratories, Report 405; 1943.
[5] Mott NF. Fragmentation of shell cases. Proc Royal Soc London Series A Math Phys Sci 1947;189(1018):300–8.
[6] Grady DE, Hightower MM. Natural fragmentation of exploding cylinders; 1990. Medium: X; Size: Pages: (13 p).
[7] Anderson Jr CE, Predebon WW, Karpp RR. Computational modeling of explosive-filled cylinders. IJES 1985;23(12):1317–30.
[8] Predebon WW, Smothers WG, Anderson CE. Missile warhead modeling: computations and experiments. Menmorandum, Report No. 2796; 1977.
[9] Gold VM, Baker EL, Poulos WJ, et al. PAFRAG modeling of explosive fragmentation munitions performance. Int J Impact Eng 2006;33(1–12):294–304.
[10] Arnold W, Rottenkolber E. Fragment mass distribution of metal cased explosive charges. Int J Impact Eng 2008;35(12):1393–8.
[11] Hutchinson MD. Replacing the equation of Fano and Fisher for cased charge blast impulse-II-fracture strain method. Propell Explos Pyrotechn 2012;37(5):605–8.
[12] Hutchinson MD. Replacing the equations of Fano and Fisher for cased charge blast equivalence – I ductile casings. Propell Explos Pyrotechn 2011;36(4):310–3.
[13] Hutchinson MD. The escape of blast from fragmenting munitions casings. Int J Impact Eng 2009;36(2):185–92.
[14] Stronge WJ, Ma X, Zhao L. Fragmentation of explosively expanded steel cylinders. IJMS 1989;31(11–12):811–23.
[15] Martineau RL, Anderson CA, Smith FW. Expansion of cylindrical shells subjected to internal explosive detonations. ExM 2000;40(2):219–25.
[16] Ivanov AI, Syrunin MA, Fedorenko AG, et al. Blasting fragmentation of spherical shells under internal explosion loading. PrPro 2001;33(2):78–87.
[17] Szyndel MDE, Collard AD, Eyre JR. A simple relation between the detonation velocity of an explosive and its Gurney energy. Propell Explos Pyrotechn 2002;27(6):365–8.
[18] Zhang Q, Miao C-Q, Lin D-C, et al. Relation of fragment with air shock wave intensity for explosion in a shell. Int J Impact Eng 2003;28(10):1129–41.
[19] Grady DE, Olsen ML. A statistics and energy based theory of dynamic fragmentation. Int J Impact Eng 2003;29(1–10):293–306.
[20] Zecevic B, Terzic J, Catovic A. Influence of warhead case material on natural fragmentation performances. In: 15th DAAAM international symposium, Vienna, Austria; 2004.
[21] Predrag Elek, Slobodan J. Modeling of fragmentation of rapidly exploding cylinders. Theor Appl Mech 2005;32(2):113–30.
[22] Zhou F, Molinari JF, Ramesh KT. An elastic–visco-plastic analysis of ductile expanding ring. Int J Impact Eng 2006;33(1–12):880–91.
[23] Zhou F, Molinari J-F, Ramesh KT. Analysis of the brittle fragmentation of an expanding ring. Comput Mater Sci 2006;37(1–2):74–85.
[24] Goto DM, Becker R, Orzechowski TJ, et al. Investigation of the fracture and fragmentation of explosively driven rings and cylinders. Int J Impact Eng 2008;35(12):1547–56.
[25] Guilkey JE, Harman TB, Banerjee B. An Eulerian–Lagrangian approach for simulating explosions of energetic devices. Comput Struct 2007;85(11-14):660–74.
[26] Glanville JP, Fairlie G, Hayhurst C, et al. Numerical simulation of fragmentation using AUTODYN-2D & 3D in explosive ordnance safety assessment. In: 6th PARARI International Explosive Ordnance Symposium, Canberra, Australia; 2003.
[27] Tham CY. Numerical simulation on the interaction of blast waves with a series of aluminum cylinders at near-field. Int J Impact Eng 2009;36(1):122–31.
[28] Tanapornraweekit G, Kulsirikasem W. Effects of material properties of warhead casing on natural fragmentation performance of high explosive (HE) warhead. World Academy of Science, Engineering and Technology; 2011.
[29] Century Dynamics. Release 14.0 documentation for ANSYS AUTODYN. ANSYS Inc., USA; 2011.
[30] Hayhurst CJ, Clegg RA. Cylindrically symmetric SPH simulations of hypervelocity impacts on thin plates. Int J Impact Eng 1997;20(1–5):337–48.
[31] Wang W, Huang Y, Grujicic M, et al. Study of impact-induced mechanical effects in cell direct writing using smooth particle hydrodynamic method. J Manufact Sci Eng Trans ASME 2008;130(2):0210121–02101210.
[32] Varas D, Zaera R, López-Puente J. Numerical modelling of the hydrodynamic ram phenomenon. Int J Impact Eng 2009;36(3):363–74.
[33] Xin-Zheng W, Song-lin Z, Guang-ping Z. Numerical analysis on fragmentation properties of the steel cylinder subjected to detonation of internal short cylindrical explosive charge. Chin J High Pressure Phys 2010;24(1):61–6.
[34] Sauer M. Simulation of high velocity impact in fluid-filled containers using finite elements with adaptive coupling to smoothed particle hydrodynamics. Int J Impact Eng 2011;38(6):511–20.
[35] Wang X, Zheng Y, Liu H, et al. Numerical study of the mechanism of explosive/impact welding using Smoothed Particle Hydrodynamics method. Mater Des 2012;35:210–9.
[36] Monaghan JJ, Gingold RA. Shock simulation by the particle method SPH. JCoPh 1983;52(2):374–89.
[37] Corbett BM. Numerical simulations of target hole diameters for hypervelocity impacts into elevated and room temperature bumpers. Int J Impact Eng 2006;33(1–12):431–40.
[38] Johnson GR, Cook WH. A constitutive model and data for metals subjected to large strain, high strain rates and high temperatures. In: The 7th international symposium on ballistic, Netherlands: Hague; 1983.